



1 **r.avaflow v1, an advanced open source computational frame-**
2 **work for the propagation and interaction of two-phase mass**
3 **flows**

4 ***Martin Mergili^{1,2}, Jan-Thomas Fischer³, Julia Krenn^{1,4} and Shiva P. Puda-***
5 ***saini⁵***

6 ¹ Institute of Applied Geology, University of Natural Resources and Life Sciences (BOKU), Peter-
7 Jordan-Straße 70, 1190 Vienna, Austria

8 ² Geomorphological Systems and Risk Research, Department of Geography and Regional Research,
9 University of Vienna, Universitätsstraße 7, 1190 Vienna, Austria

10 ³ Department of Natural Hazards, Austrian Research Centre for Forests (BFW), Rennweg 1, 6020
11 Innsbruck, Austria

12 ⁴ Group Roads, Provincial Government of Lower Austria, Landhausplatz 1/17, 3109 St. Pölten,
13 Austria

14 ⁵ Department of Geophysics, University of Bonn, Meckenheimer Allee 176, 53115 Bonn, Germany

15 Correspondence to: M. Mergili (martin.mergili@boku.ac.at)

16 **Abstract**

17 r.avaflow represents an innovative open source computational tool for routing rapid mass flows,
18 avalanches or process chains from a defined release area down an arbitrary topography to a depo-
19 sition area. In contrast to most existing computational tools, r.avaflow (i) employs a two-phase,
20 interacting solid and fluid mixture model; (ii) is suitable for modelling more or less complex pro-
21 cess chains and interactions; (iii) explicitly considers both entrainment and stopping i.e. the
22 change of the basal topography; (iv) allows for the definition of multiple release masses and/or hy-
23 drographs; and (v) serves with built-in functionalities for validation, parameter optimization and
24 sensitivity analysis. r.avaflow is freely available as a raster module of the GRASS GIS software,
25 employing the programming languages Python and C along with the statistical software R. We
26 exemplify the functionalities of r.avaflow by means of two sets of computational experiments: (1)
27 generic process chains consisting in bulk mass and hydrograph release into a reservoir with en-
28 trainment of the dam and impact downstream; (2) the prehistoric Acheron rock avalanche, New
29 Zealand. The simulation results are generally plausible for (1) and, after the optimization of two
30 key parameters, reasonably in line with the corresponding observations for (2). However, we
31 identify some potential to enhance the analytic and numerical concepts. Further, thorough pa-
32 rameter studies are necessary in order to make r.avaflow fit for reliable forward simulations of
33 possible future mass flow events.

34 **Keywords:** GIS raster analysis, mass flows, open source, process chains, two-phase flow model



35 1 Introduction

36 Rapid flows or avalanches of snow, debris, rock or ice, or processes, process chains or process in-
37 teractions involving more than one type of movement or material frequently lead to loss of life,
38 property and infrastructures in mountainous areas worldwide. All state-of-the-art methods for
39 anticipating the occurrence, characteristics, and dynamics of such events rely on computer simula-
40 tions. On the one hand, models attempt to identify those areas where mass flows are likely to re-
41 lease (landslide susceptibility; Guzzetti, 2006; Van Westen et al., 2006). On the other hand, they
42 attempt to anticipate the motion of rapid mass flows once they are released (Hungr et al., 2005a).
43 Whilst conceptual models (Lied and Bakkehøi, 1980; Gamma, 2000; Wichmann and Becht, 2003;
44 Horton et al., 2013; Mergili et al., 2015) are employed to identify possible impact areas at broad
45 scales, physically-based dynamic models are used for the detailed back-analysis or prediction of
46 specific events.

47 Advanced fluid dynamics offers a broad array of physically-based dynamic modelling approaches
48 for mass flows, mostly referred to as granular avalanches or debris flows. Such models often centre
49 on 2D “shallow flow” equations, but they vary considerably among themselves in terms of their
50 concept, complexity and capacity to model specific types of phenomena. Voellmy (1955) pio-
51 neered mass flow modelling, followed by the work of Grigoriyan et al. (1967); Savage and Hutter
52 (1989); Takahashi (1991); Iverson (1997); Pitman and Le (2005); and many others (see Pudasaini
53 and Hutter, 2007 for a review). Savage and Hutter (1989) introduced depth-averaged mass and
54 momentum conservation equations which were later utilized, modified and extended by Mangen-
55 ey et al. (2003, 2005); Denlinger and Iverson (2004); and McDougall and Hungr (2004, 2005). The
56 Savage and Hutter (1989) model was further extended to include the effects of pore fluid by Iver-
57 son and Denlinger (2001); Savage and Iverson (2003); Pitman and Le (2005); Pudasaini et al.
58 (2005); Pastor al. (2009); and Hutter and Schneider (2010a, b). Still, these approaches either repre-
59 sent effectively one-phase models, or do not fully consider the two-phase nature of most mass
60 flows. Pudasaini (2012) introduced a general two-phase mass flow model including several essen-
61 tially new physical aspects of two-phase solid-fluid mixture flows. In comparison to one phase
62 models, this amongst few other (e.g. Kowalski and McElwaine, 2013) two-phase approaches ap-
63 pears suitable for the realistic simulation of most types of process chains and interactions.

64 Entrainment of the basal material into the flow may substantially alter the dynamics and charac-
65 teristics of mass flows, increasing their destructive potential (Hungr and Evans, 2004; Hungr et al.,
66 2005b; Reid et al., 2011; Berger et al., 2011; Pirulli and Pastor, 2012). Empirical laws for entrain-
67 ment were proposed by Rickenmann et al. (2003); McDougall and Hungr (2005); and Chen et al.
68 (2006), whereas mechanical concepts were introduced by Fraccarollo and Capart (2002); Pitman et
69 al. (2003a); Sovilla et al. (2006); Medina et al. (2008); and Iverson (2012). The available entrain-
70 ment models are effectively single-phase, and developed for bulk debris (Armanini et al., 2009;
71 Crosta et al., 2009; Hungr and McDougall, 2009; Pirulli and Pastor, 2012). Whilst the importance
72 of erosion, and the associated change of the basal topography (Fraccarollo and Capart, 2002; Hungr
73 and Evans, 2004; Hungr et al., 2005b; Le and Pitman, 2009) has been recognized by the scientific
74 community, attempts to simulate deposition of mass flow material are sparsely documented.



75 Various types of numerical schemes have been used to solve mass flow model equations in order to
76 redistribute mass and momentum (e.g., Davis, 1988; Toro, 1992; Nessayahu and Tadmor, 1990;
77 Wang et al., 2004). Previously, equations were commonly formulated and solved for pre-defined
78 types of topographies (Pudasaini et al., 2005, 2008; Wang et al., 2004) whereas a mathematically
79 consistent application to arbitrary mountain topographies – and therefore to real-world conditions
80 – still remains a challenge (Mergili et al., 2012). This issue is closely related to the fact that the
81 model equations are commonly expressed in topography-following coordinates hardly compatible
82 with Geographic Information Systems (GIS). Nevertheless, some of the mass flow models men-
83 tioned have been implemented in computational tools used for hazard mapping and zoning, such
84 as DAN (Hungri et al., 1995); TITAN2D (Pitman et al., 2003b; Pitman and Le, 2005); SamosAT
85 (Sampl and Zwinger, 2004); or RAMMS (Christen et al., 2010a, b). Hergarten and Robl (2015) de-
86 veloped a modelling tool relying on the open source flow solver GERRIS (Popinet, 2009).

87 None of these models serves for explicitly simulating stopping and deposition, nor for simulating
88 chains or interactions of two-phase mass flows. There is, however, a particular need to appropri-
89 ately consider process chains and interactions in mass flow simulations: some of the most destruc-
90 tive events in history have evolved from cascading effects, such as the 1970 Huascarán event in
91 Peru (Evans et al., 2009) or the 2002 Kolka-Karmadon event in Russia (Huggel et al., 2005).

92 The present work addresses some of the needs and issues raised by introducing the multi-
93 functional open source computational framework `r.avaflow`, employing an enhanced version of
94 the Pudasaini (2012) two-phase flow model for routing mass flows from a defined release area
95 down arbitrary topography to a deposition area. Next, we introduce the structure and functionali-
96 ties of `r.avaflow` (Sect. 2). Then we perform two computational experiments in order to demon-
97 strate the functionalities of the computational framework (Sect. 3). We discuss the implementa-
98 tion of `r.avaflow` and the implications of our findings (Sect. 4), and finally conclude with the key
99 messages of the work and a brief outlook to the next steps (Sect. 5).

100 **2 The computational framework `r.avaflow`**

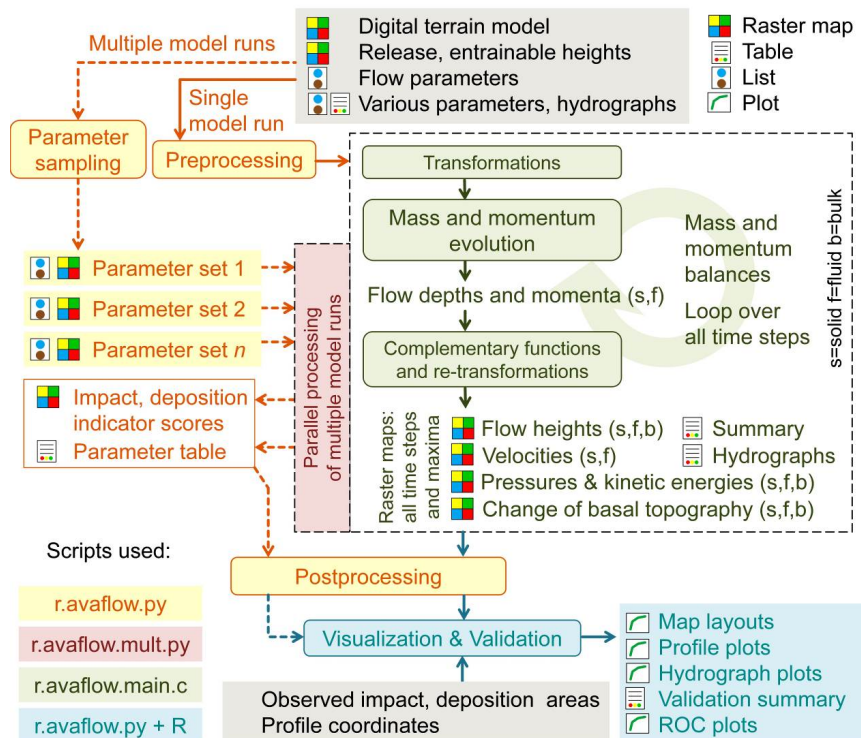
101 **2.1 Computational implementation**

102 `r.avaflow` computes the propagation of mass flows from one or more given release areas over a giv-
103 en basal topography until (i) all the material has stopped and deposited; (ii) all the material has left
104 the area of interest; or (iii) a user-defined maximum simulation time has been reached. `r.avaflow` is
105 developed along two lines with regard to its software environment and operation, `r.avaflow` [EX-
106 PERT] and `r.avaflow` [PROFESSIONAL]. The present work refers to `r.avaflow` [EXPERT] which is
107 implemented as a raster module of the open source software package GRASS GIS 7 (Neteler and
108 Mitasova, 2007; GRASS Development Team, 2016). We use the Python programming language for
109 data management, pre-processing and post-processing tasks (module `r.avaflow`). The flow propaga-
110 tion procedure (see Sect. 2.3 and 2.4) is written in the C programming language (sub-module
111 `r.avaflow.main`). Together with Python, the R software environment for statistical computing and



112 graphics (R Core Team, 2016) is employed for built-in validation and visualization functions.
 113 Fig. 1 illustrates the logical framework of r.avaflow.

114 Multiple model runs may be executed in parallel, exploiting all computational cores available (see
 115 Sect. 2.5). This speeds up the processing considerably, and allows the use of r.avaflow on computa-
 116 tional clusters. Parallelization is implemented at the Python level (Mergili et al., 2014, 2015): for
 117 each model run a batch file is produced within the module r.avaflow. This batch file calls the Py-
 118 thon-based sub-module r.avaflow.mult, launching r.avaflow.main which is then executed with the
 119 specific parameters for the associated model run. Thereby, the Python library “Threading”, a high-
 120 er-level threading interface is exploited. The Python class “Queue” is employed for handling the
 121 queue of items to be processed.



122
 123 Figure 1 Logical framework of r.avaflow. The transformations and re-transformations refer to the
 124 conversion of heights and GIS coordinates to depths and topography-following coordinates, and
 125 vice versa (see Sect. 2.3).

126 r.avaflow was developed and tested with the operating systems (OS) Ubuntu 12.04 LTS and
 127 16.04 LTS, and Scientific Linux 6.6 (Red Hat). It is expected to work on other UNIX systems, too.
 128 A simple user interface is available. However, the tool may be started more efficiently through
 129 command line parameters, enabling a straightforward batching on the shell script level. This fea-
 130 ture facilitates model testing and the combination with other GRASS GIS modules.

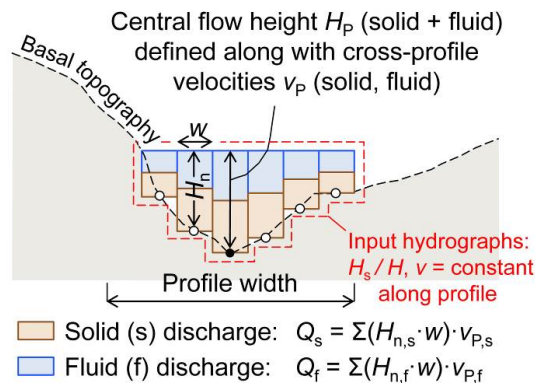


131 All experiments where parallel processing is not applied are performed on an Intel® Core i7 975
 132 with 3.33 GHz and 16 GB RAM (DDR3, PC3-1333 MHz), exploring a maximum of eight cores
 133 through hyperthreading and using the OS Ubuntu 12.04 LTS. All experiments with parallel pro-
 134 cessing are performed on the Vienna Scientific Cluster, serving with approx. 2020 nodes (Super-
 135 micro X9DRD-iF Board), each equipped with two Intel Xeon E5-2650v2 with 2.6 GHz und
 136 8 · 8 GB RAM. The OS for these computations is Scientific Linux 6.6 (Red Hat).

137 2.2 Input and output

138 The key input parameters of r.avaflow are summarized in Table 1. Essentially, r.avaflow relies on
 139 (i) a digital terrain model (DTM) representing the elevation of the basal surface before the event
 140 under investigation; (ii) raster maps of the spatial distribution of the solid and fluid release heights
 141 or hydrographs of solid and fluid release; (iii) a set of flow parameters (Table 2). Input raster maps
 142 of the entrainable solid and fluid heights, and a raster map or value defining the empirical en-
 143 trainment coefficient (needed for entrainment) are optional. Instead of the solid and fluid release
 144 and entrainable heights, the total heights and global values of the solid concentration may be de-
 145 fined.

146 There is no restriction imposed on the arrangement of the release pixels. Patches with pixels
 147 where the release height is larger than zero may be defined in various parts of the investigation
 148 area. An arbitrary number of release hydrographs – each associated to a given set of coordinates –
 149 can be defined alternatively or in addition to the release mass. This allows the simulation of com-
 150 plex interactions between different types of processes (see Sect. 3). Hydrographs are defined
 151 through their solid and fluid heights at the centre point of the hydrograph profiles, and by the sol-
 152 id and fluid flow velocities. The flow height distribution along the hydrograph profile – which
 153 should be aligned perpendicular to the main flow direction – is derived from the assumptions of a
 154 horizontal cross section of the flow table and a maximum profile length (Fig. 2).



155
 156 Figure 2 Sketch of a hydrograph profile. The flow surface of input hydrographs is defined by H_p
 157 and is extended in cross-profile direction either to the edge of the profile or until it intersects with
 158 the basal topography.



159 Table 1 Key input and output parameters of r.avaflow. s = solid; f = fluid; b = bulk. Remarks: 1 –
 160 mandatory; 2 – one of the input data sets A, B or C+D is mandatory, C+D may also be provided in
 161 addition to A or B; $m_D \geq n_C$, if $m_D > n_C$ the remaining sets of D are output hydrographs; 3 – either A
 162 or B may be provided if entrainment is activated, otherwise all values of $H_{E_{max}} = \infty$; C is mandatory
 163 with entrainment; 4 – at least one of the data sets A, B and C is mandatory for validation.

Parameter	Symbol	Unit	Format	Remarks
Input				
Initial elevation of basal surface	Z_0	m	Raster map	1
s, f release heights	$H_{0,s}, H_{0,f}$	m, m	Raster maps	2A
Total release height, s concentration of release mass	H_0, α_{s0}	m, –	Raster map, value	2B
s, f entrainable heights	$H_{E_{max},s}, H_{E_{max},f}$	m, m	Raster maps	3A
Entrainable total height, s concentration of entrainable mass	$H_{E_{max}}, \alpha_{s,E_{max}}$	m, –	Raster map, value	3B
n_C hydrograph tables: s and f flow heights and velocities at defined points of time (see Fig. 2)	$H_{P,s}, v_{P,s}, H_{P,f}, v_{P,f}$	m, m s ⁻¹ m, m s ⁻¹	Tables	2C
m_D sets of centre coordinates, length and aspect of hydrograph	–	m, degree	Sets of four values	2D
Flow parameters (see Table 2)	–	–	Set of 14 values	1
Basal surface parameters (see Table 2)	–	–	Set of 2 values	3C
Time interval for output, max. time after which simulation terminates	$\Delta t_{out}, t_{term}$	s, s	Set of 2 values	1
Threshold flow height for visualization and validation	H	M	Value	1
Observed impact area, observed deposition area	OIA, ODA	–, –	Raster maps	4A, B
Vertex coordinates of flow path	–	M	Even number of ≥ 4 values	4C
Output (excluding validation and visualization output; see Sect. 2.6)				
Maximum flow height, kinetic energy, and pressure (each for s, f, b)	$H_{Max}, T_{Max}, p_{Max}$	m, Pa, J	Raster maps	Always
Flow height, flow kinetic energy, and flow pressure at each output time step t_{out} (each for s, f, b)	$H_{t_{out}}, T_{t_{out}}, p_{t_{out}}$	m, Pa, J	Raster maps	Always
Total release height, solid concentration of release mass (each for s, f)	$v_{x,n}, v_{y,n}, v_n$	m s ⁻¹	Raster maps,	Always
Change of basal topography, height of final deposition (s,f,b)	E_n, H_D	m, m	Raster maps	If >0
Impact indicator index, deposition indicator index	III, DII	–, –	Raster maps	Multiple runs
$m_D - n_C$ output hydrograph tables: s and f flow heights, velocities and discharges at defined points of time	$H_{P,s}, v_{P,s}, Q, H_{P,f}, v_{P,f}, Q$	Various	Tables	If $m_D > n_C$



164 Mandatory parameters further include the time interval at which output maps are written Δt_{out} (s),
165 the maximum time after which the simulation terminates, and the threshold flow height for visu-
166 alization and validation H_t (m; see Table 1). Optional parameters further include raster maps of the
167 observed impact area and deposition height as well as a set of flow path coordinates (for validation
168 and visualization; see Fig. 1 and Sect. 2.6). An exhaustive list of input parameters is provided in the
169 user manual of r.avafLOW, available at <http://www.avafLOW.org/software.html>.

170 If a single model run is executed (see Fig. 1), the output of r.avafLOW consists in raster maps of sol-
171 id, fluid and total flow heights, flow velocities in x and y direction and in absolute terms, pressures
172 and kinetic energies, and the change of the basal topography (only relevant with entrainment or
173 stopping; see Sect. 2.4). All raster maps are produced for each output time step (defined by Δt_{out})
174 and for the maximum over all time steps. Further, a table summarizing the maximum solid and
175 fluid flow heights and velocities as well as flow volumes and kinetic energies for all output time
176 steps is produced. Optionally, solid and fluid output hydrographs are generated for an arbitrary
177 number of given output hydrograph profiles (see Table 1 and Fig. 2). With multiple model runs,
178 the results of each single run are aggregated to indices (see Sect. 2.5). In the present work we focus
179 on the output heights, hydrographs and indices when analyzing the results, rather than on veloci-
180 ties, or deduced results such as pressures or kinetic energies (see Sect. 3).

181 2.3 Mass and momentum evolution

182 The core functionality of r.avafLOW consists in the redistribution of mass and momentum, employ-
183 ing a dynamic flow model and a numerical scheme. Thereby the tool offers implementations of
184 the Voellmy-Salm one-phase flow model (Christen et al., 2010a, b) and of a slightly enhanced ver-
185 sion of the Pudasaini (2012) two-phase flow model. In the present work we only consider the lat-
186 ter implementation. It builds on the conservation of mass and momentum, computed separately
187 but simultaneously for the solid and fluid components of the flow. A system of six differential
188 equations (expressed in locally topography-following coordinates) represents the basis for a set of
189 six flux and source terms, regarding solid and fluid flow depths (D_s , D_f), solid momentum M_s and
190 fluid momentum M_f in x direction ($M_{sx} = D_s \cdot v_{sx}$, $M_{fx} = D_f \cdot v_{fx}$), and M_s and M_f in y direction
191 ($M_{sy} = D_s \cdot v_{sy}$, $M_{fy} = D_f \cdot v_{fy}$), where v is flow velocity.

192 The Pudasaini (2012) model employs the Mohr-Coulomb plasticity for the solid stress. The fluid
193 stress is modelled as a solid-volume-fraction-gradient-enhanced non-Newtonian viscous stress.
194 The generalized interfacial momentum transfer includes viscous drag, buoyancy, and virtual mass
195 induced by relative acceleration between the phases. A new, generalized drag force is proposed
196 that covers both solid-like and fluid-like contributions. Strong coupling between the solid- and
197 the fluid-momentum transfer leads to simultaneous deformation, mixing, and separation of the
198 phases. Inclusion of the non-Newtonian viscous stresses is important in several aspects. The advec-
199 tion and diffusion of the solid volume fraction play an important role. The model includes a num-
200 ber of innovative, fundamentally new, and dominant physical aspects. Please consult Pudasaini
201 (2012) for the full details of the model, including the corresponding equations. The flow param-
202 eters required are summarized in Table 2.



203 Solving the differential equations and propagating the flow from one pixel to the next requires the
 204 implementation of a numerical scheme. For this purpose r.avaflow employs a high resolution Total
 205 Variation Diminishing Non-Oscillatory Central Differencing (TVD-NOC) Scheme, a numerical
 206 scheme useful to avoid unphysical numerical oscillations (Nessyahu and Tadmor, 1990). Cell aver-
 207 ages of all six state variables are computed using a staggered grid: the system is moved half of the
 208 cell size with every time step, the values at the corners of the cells and in the middle of the cells
 209 are computed alternatively at half and full time steps, respectively. The TVD-NOC scheme with
 210 the Minmod limiter has successfully been applied to a large number of mass flow problems (Tai et
 211 al., 2002; Wang et al., 2004; Mergili et al., 2012; Pudasaini and Krautblatter, 2014; Kafle et al.,
 212 2016; Kattel et al., 2016).

213 Table 2 Flow and basal surface parameters of r.avaflow. The basal surface parameter C_E is used for
 214 computing the entrainment (see Sect. 2.4); all other parameters listed represent flow parameters
 215 required with the enhanced version of the Pudasaini (2012) two-phase flow model. Exp. 1 and 2
 216 refer to the values used for the computational experiments introduced in Sect. 3.

Symbol	Parameter	Unit	Exp. 1A, B, C	Exp. 2A, B
ρ_s	Solid material density	kg m ⁻³	2700	2700
ρ_f	Fluid material density	kg m ⁻³	1000	1000
φ	Internal friction angle	De- gree	35	35
δ	Basal friction angle ¹⁾	De- gree	20	15–25, 17
C_{VM}	Virtual mass	–	0.5	0.5
v_T	Terminal velocity	m s ⁻¹	1	1
P	Parameter for combination of solid- and fluid-like contributions to drag resistance	–	0.5	0.5
Re_p	Particle Reynolds number	–	1	1
J	exponent for drag (1 = linear, 2 = quadratic)	–	1	1
N_R	Quasi Reynolds number	–	30,000	30,000
N_{RA}	Mobility number	–	1,000	1,000
χ	Viscous shearing coefficient for fluid	–	0	0
ξ	Solid concentration distribution with depth	–	0	0
C_{AD}	Ambient drag coefficient ²⁾	–	0	0
C_E	Entrainment coefficient ¹⁾	kg ⁻¹	–, 10 ^{-5.3} , 10 ^{-6.0}	–

217 ¹⁾ Alternatively, these parameters may be provided as raster maps instead of global values; ²⁾ Refer
 218 to Kattel et al (2016) for ambient drag

219 The input and output of r.avaflow (see Sect. 2.2) is discretized on the basis of GIS raster pixels, rec-
 220 tangular in shape in the ground projection. The grid spacing in x and y directions, and the pixel
 221 area, are corrected for the local slope in order to maintain consistency with the state variables ex-
 222 pressed in topography-following coordinates. Gravitational acceleration in the topography-
 223 following x, y, and z directions – representing a fundamental input to the Pudasaini (2012) model
 224 – is computed from the DTM, employing a central differencing scheme. All input heights H (m)
 225 are expressed in vertical direction. They are converted into depths D (m) expressed in direction
 226 normal to the local topography as in the Pudasaini (2012) model formulation. The resulting depths



227 are converted into heights for output. An adaptation is applied to utilize the TVD-NOC Scheme
 228 which is meant for equidistant quadratic cells. The time step length Δt (s) is dynamically updated
 229 according to the CFL condition (Courant et al., 1967; Wang et al., 2004).

230 2.4 Complementary functions

231 Table 3 summarizes some additional functions of r.avaflow. The first three functions in the table
 232 are introduced for numerical purposes. Entrainment and stopping, in contrast, represent dynamic
 233 functions not covered by the Pudasaini (2012) model and are executed independently of the nu-
 234 merical scheme at the end of each time step (see Fig. 1). Even though the separation of these func-
 235 tions from the numerical scheme can be questioned physically and mathematically, we consider
 236 the current implementation a reasonable first approximation (see Sect. 4). We now elaborate the
 237 concepts employed for entrainment and stopping in more detail.

238 Table 3 Functionalities of r.avaflow introduced for numerical purposes (ID 1–3) or complementing
 239 the Pudasaini (2012) model (ID 4,5). Exp. 1 and 2 refer to the computational experiments intro-
 240 duced in Sect. 3; Y = activated; N = deactivated.

ID	Function	Description	Exp. 1ABC	Exp. 2AB
1	Diffusion control	Propagation of the flow from one pixel to the next is suppressed if the velocity is not high enough, reducing numerical diffusion	YYY	YY
2	Conservation of volume	Flow volume lost due to numerical reasons is replaced through an increase of D of all pixels by the fraction of lost volume after each time step	YYY	YY
3	Surface control	Numerical oscillations of undisturbed flat surfaces (such as reservoirs) are avoided	YYY	NN
4	Entrainment	Empirical approach to compute entrainment of basal material	NYY	NN
5	Stopping and deposition	Energy balance approach for stopping and deposition of flow material	NNN	YY

241

242 The potential solid and fluid entrainment rates $q_{E,s}$ and $q_{E,f}$ (m s^{-1} ; expressed perpendicular to the
 243 basal topography) build on the user-defined empirical entrainment coefficient C_E (kg^{-1}) (see Ta-
 244 ble 2) and the solid and fluid momenta. We assume a vertically homogeneous solid fraction within
 245 the entrainable material, which is reflected in the ratio between $q_{E,s}$ and $q_{E,f}$:

$$246 \quad q_{E,s} = C_E |M_s + M_f| \alpha_{s,E_{\max}}, \quad q_{E,f} = C_E |M_s + M_f| (1 - \alpha_{s,E_{\max}}). \quad (1)$$

247 The fact that the basal velocities, which are relevant for entrainment, are lower than the depth-
 248 averaged velocities is not explicitly considered, but has to be reflected in the value of C_E . $q_{E,s}$ and



249 $q_{E,f}$ are always positive. Consequently, the solid and fluid changes of the basal topography $H_{E,s}$ and
 250 $H_{E,f}$ (m) are positive for entrainment:

$$251 \quad H_{E,s,t} = \min \left(H_{E,s(t-\Delta t)} + \frac{q_{E,s} \Delta t}{\cos \beta}, H_{E_{\max,s}} \right), \quad (2)$$

$$252 \quad H_{E,f,t} = \min \left(H_{E,f(t-\Delta t)} + \frac{q_{E,f} \Delta t}{\cos \beta}, H_{E_{\max,f}} \right), \quad (3)$$

253 where $H_{E,s(t-\Delta t)}$ and $H_{E,f(t-\Delta t)}$ (m) are the change of the basal topography at the start of the time step,
 254 $H_{E_{\max,s}}$ and $H_{E_{\max,f}}$ (m) are the maximum entrainable depths at the given pixel, t (s) is the time
 255 passed at the end of the time step, Δt (s) is the time step length, and β is the local slope of the basal
 256 surface. The division by $\cos \beta$ accounts for the conversion from depths to heights. The solid and
 257 fluid entrained depths $D_{E,s} = (H_{E,s,t} - H_{E,s(t-\Delta t)}) \cos \beta$ and $D_{E,f} = (H_{E,f,t} - H_{E,f(t-\Delta t)}) \cos \beta$ are added to the
 258 solid and fluid flow depths. We further assume that entrainment increases the solid and fluid mo-
 259 mentum of the flow in each direction by the product of the entrained solid and fluid depth and
 260 the bulk velocity in the given direction (M_E ; Fig. 3a). The basal topography and, consequently, the
 261 x and y pixel sizes, pixel areas, and gravitational acceleration components in x, y, and z direction
 262 are updated after each time step.

263 The changes in gravitational acceleration also influence the magnitude of the frictional terms,
 264 which are important for stopping processes. In the literature few approaches explicitly consider
 265 stopping processes directly in their numerical scheme by operator splitting methods coupled with
 266 the determination of admissible stresses (e.g. Mangeney et al., 2003; Zhai et al., 2015). Here, in
 267 order to consider stopping, we choose a different approach by proposing the dimensionless factor
 268 of mobility FoM , relating the distance required for stopping s_{stop} to the numerical spatial resolution
 269 Δs in the direction of movement. The flow stops if $s_{\text{stop}} \leq \Delta s$ i.e. $FoM \leq 1$ (see Fig. 3b):

$$270 \quad FoM = \frac{s_{\text{stop}}}{\Delta s}. \quad (4)$$

271 To estimate s_{stop} we formulate the energy balance considering that the initial kinetic energy at an
 272 initial velocity v_0 (m s^{-1}) and the change of potential energy while travelling the distance s_{stop} have
 273 transformed in dissipative energy due to Coulomb friction, which dominates close to stopping.
 274 With this the energy balance estimate yields:

$$275 \quad \frac{v_0^2}{2} + s_{\text{stop}} \sin \beta_v g = s_{\text{stop}} \tan \delta \cos \beta_v g. \quad (5)$$

276 Consequently,

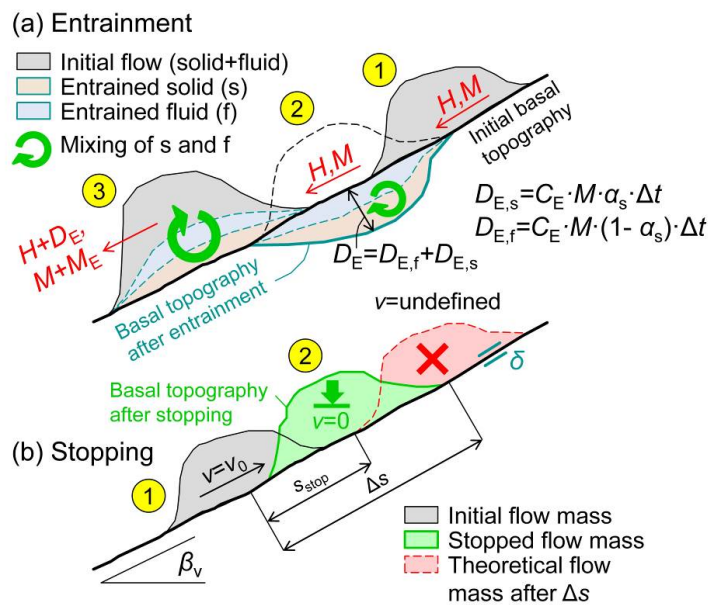
$$277 \quad s_{\text{stop}} = \frac{v_0^2}{2g \cos \beta_v (\tan \delta - \tan \beta_v)}, \quad (6)$$

278 where δ is the basal friction angle, β is the slope angle in the direction of movement, and g (m s^{-2})
 279 is gravitational acceleration (see Table 2). According to Eq. 6 the stopping distance s_{stop} is positive



280 for $\delta > \beta$, meaning that stopping is possible when the friction angle is higher than the slope angle
 281 i.e., in particular at flat or even counter slopes. We note that, by a simple transformation of Eq. 6,
 282 FoM can alternatively be derived by relating the stopping time to the time step length.

283 FoM can relate to various spatial units: (i) a single pixel i.e., FoM is computed separately for each
 284 pixel. It may happen that stopping of the flow occurs at a certain pixel, but not at its neighbour
 285 pixels. (ii) v_0 and β are averaged over a certain pixel neighbourhood to compute FoM , so that
 286 stopping occurs at patches of adjacent pixels. (iii) β and the associated component of v are aver-
 287 aged over the entire area of interest. This means that the entire flow stops at once.



288 Figure 3 Interactions of the flow with the basal topography: (a) entrainment, assuming that $H_{E_{max,s}}$
 289 and $H_{E_{max,f}}$ are not limiting; D_E = entrained depth; (b) stopping. Both panes represent sections along
 290 the steepest slope of the basal topography.
 291

292 The third possibility is currently implemented with `r.avafLOW` as an optional function. If activated,
 293 the simulation terminates as soon as stopping occurs and the basal topography is lifted by $H_s + H_f$.
 294 Note that, in the current implementation, stopping always considers the bulk mass, without dif-
 295 ferentiating between the solid and the fluid components. This simplification is reasonable for
 296 flows characterized by a relatively small fluid volume fraction.

297 2.5 Multiple model runs

298 `r.avafLOW` includes a built-in function to perform multiple model runs at a time with controlled or
 299 random variation of uncertain input parameters between given lower and upper thresholds. Es-
 300 sentially, this concerns the flow parameters (see Table 2), but also the solid concentration of the
 301 release mass α_0 . Multiple parameters can be varied at a time. This procedure serves for two pur-
 302 poses:



- 303 • It facilitates multi-parameter sensitivity analysis & optimization efforts;
- 304 • The results of all model runs are aggregated to an impact indicator index (*III*) and a deposi-
- 305 tion indicator index (*DII*), each in the range 0–1. *III* represents the fraction of model runs
- 306 where $H_{Max} \geq H$ at a given pixel whilst *DII* represents the fraction of model runs where
- 307 $H_D \geq H$ at a given pixel. *III* and *DII* can be used to demonstrate the impact of uncertain
- 308 input parameters on the simulation result.
- 309 The model runs can be split among multiple computational cores (parallel processing), enabling
- 310 the exploitation of high-performance computational environments (see Sect. 2.1).

311 2.6 Validation and visualization

312 r.avaflow can be used to produce map layouts and animations of the key results (see Fig. 1). It fur-

313 ther includes built-in functions to validate the model results against observations. Validation relies

314 (i) on the availability of a raster map of the observed impact or deposition area of the event under

315 investigation, (ii) on a user-defined profile along the main flow path (see Table 1), or (iii) on

316 measurements H or v at selected coordinates and time steps. Those pixels with observed impact or

317 deposition are referred to as observed positives (*OP*), those without observed impact or deposition

318 as observed negatives (*ON*). When using the observed impact area (OIA) as reference, all pixels

319 with $H_{Max} \geq H$ are considered as predicted positives (*PP*), all pixels with $H_{Max} < H$ are considered

320 as predicted negatives (*PN*). When using the observed deposition area (ODA) as reference, all pix-

321 els with $H_D \geq H$ are considered as PP, all pixels with $H_D < H$ are considered as PN. Intersecting

322 *ON* and *OP* with *PP* and *PN* results in four validation scores: true positive (*TP*), true negative

323 (*TN*), false positive (*FP*) and false negative (*FN*) predictions (Fig. 4). *TN* strongly depends on the

324 size of the area of interest. It is normalized to $5 \cdot (TP + FN) - FP$ in order to allow a meaningful com-

325 parison of model performance among different case studies. These scores build the basis for most

326 of the validation parameters described in Table 4. Only the excess travel distance ΔL relies on the

327 observed and simulated terminal points of the flow, based on a user-defined longitudinal profile.

328 We note that this profile is only needed for validation, but is not used for the mass flow simulation

329 itself.

330 Values of $\Delta L > 0$ and $FoC > 1$ indicate conservative results (simulated impact or deposition area is

331 larger than observed impact or deposition area) whilst values of $\Delta L < 0$ and $FoC < 1$ indicate non-

332 conservative results. *CSI*, *D2PC*, and *AUROC* do not allow to conclude on the conservativeness of

333 the results. ΔL , *FoC*, *CSI*, and *D2PC* as defined in Table 4 target at the validation of H_{Max} or H_D de-

334 rived with one single model run. With multiple model runs (see Sect. 2.5) the validation paramet-

335 ers are computed separately for each run, allowing to conclude on the sensitivity of the model

336 performance to given input parameters, or to optimize input parameter values.

337 In contrast, ROC (Receiver Operating Characteristics) curves are used to test the performance of

338 the overall output of multiple model runs. Such curves are produced for *III* (OIA as reference)

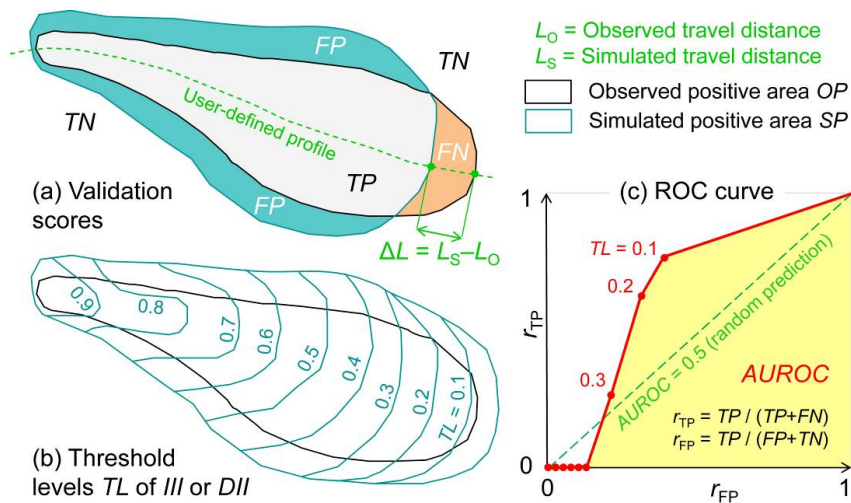
339 and/or *DII* (ODA as reference): the true positive rate is plotted against the false positive rate for

340 various levels of *III* or *DII*. The area under the curve connecting the resulting points, *AUROC*, is



341 used as an indicator for model performance ($AUROC \approx 1$ indicates an excellent performance; see
 342 Fig. 4 and Table 4).

343 Further, the difference between observed and simulated values of H and v at selected sets of coordi-
 344 nates and points of time can be analyzed. This function is mainly useful for very well-
 345 documented case studies such as laboratory experiments and is not further used in the present
 346 work.



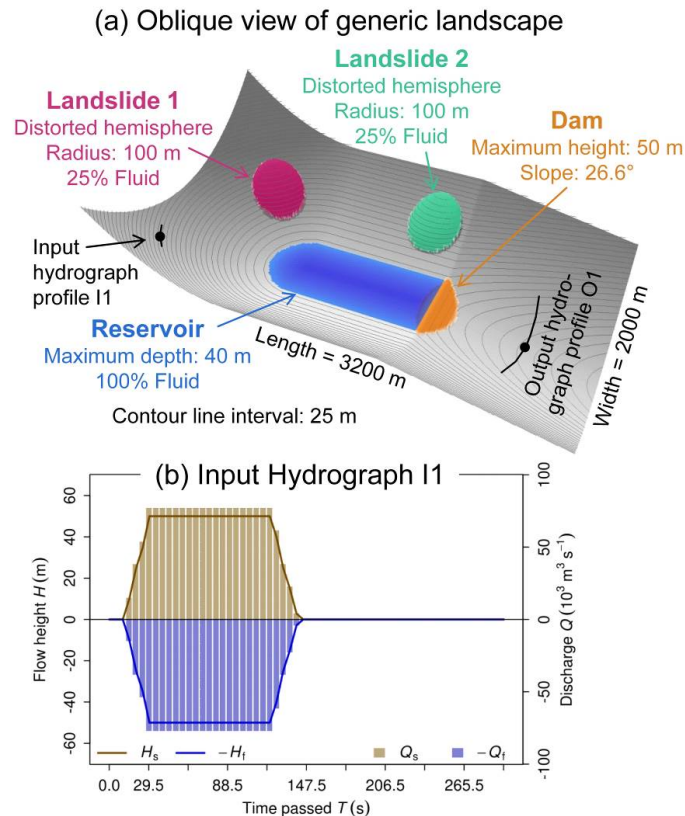
347
 348
 349

Figure 4 Validation of $r.avaflow$ results. (a) Validation scores for single model run; (b) multiple model runs: threshold levels of III or DII , employed to produce (c) ROC curves.

350 Table 4 Validation parameters used in $r.avaflow$ (see also Fig. 4). S = single model run, binary simu-
 351 lation result; M = multiple model runs, simulation result in the range 0–1. The concepts of CSI
 352 and $D2PC$ are taken from Formetta et al. (2015). All validation parameters are computed for H_{Max}
 353 (OIA as reference) and/or H_b (ODA as reference), depending on which of the reference data are
 354 available.

Scope	Name	Definition	Possible range	Optimum
S	Excess travel distance ΔL	$L_s - L_o$	$[-L_o, \infty]$	0.0
S	Factor of conservativeness FoC	$FoC = \frac{PP}{OP} = \frac{TP + FP}{TP + FN}$	$[0, \infty]$	1.0
S	Critical success index CSI	$CSI = \frac{TP}{TP + FP + FN}$	$[0, 1]$	1.0
S	Distance to perfect classi- fication $D2PC$	$D2PC = \sqrt{(1 - r_{TP})^2 + r_{FP}^2}$ $r_{TP} = \frac{TP}{OP}, r_{FP} = \frac{FP}{ON}$	$[0, 1]$	0.0
M	Area under ROC curve $AUROC$	Function of r_{TP} and r_{FP} for different levels of DII or III (see Fig. 4)	$[0, 1]$	1.0

355



356
 357 Figure 5 Generic landscape used for Experiment 1A–C. (a) Oblique view illustrating the topogra-
 358 phy and elements of the landscape. (b) Input hydrograph I1 employed for Experiment 1C.

359 3 Computational experiments

360 3.1 Experiment 1: Generic process chain

361 3.1.1 Topographic setup

362 In a first step, the potential of r.avafLOW for simulating process chains is demonstrated, considering
 363 the interaction between one or more landslides, a reservoir, and the dam impounding the reser-
 364 voir. This experiment represents a follow-up to the work of Pudasaini (2014); Kafle et al. (2016);
 365 and Kattel et al. (2016). We construct a generic landscape of size 3200 m · 2000 m, illustrated in
 366 Fig. 5a. This landscape consists of the following elements: (i) W–E stretching trough-shaped valley
 367 with an amphitheatre-shaped head, inclined towards E in its lower part; (ii) dam with a trapezoi-
 368 dal cross section running across the valley, consisting of 100% solid material; (iii) reservoir im-
 369 pounded by the dam; (iv) landslide release mass near the NW corner of the area of interest (Land-
 370 slide 1); (v) landslide release mass directly N of the dam (Landslide 2); (vi) hydrograph release of
 371 landslide near the SW corner of the area of interest; (vii) measurement profile for output hydro-



372 graph downstream from the dam. Both landslide release masses assume the shape of a hemi-
373 ellipsoid imposed on the basal topography (see Fig. 5a). The algorithm for exactly reproducing the
374 generic landscape in GRASS GIS is available at <http://www.avaflo.org/casestudies.html>.

375 3.1.2 Modelling strategy and parameterization

376 The landslides 1 and 2 consist of 75% solid and 25% fluid by volume, the input hydrograph I1 (see
377 Fig. 5b) consists of 50% each solid and fluid per volume. The parameters and settings applied are
378 summarized in the Tables 2 and 3.

379 Three computational experiments are performed, with increasing complexity from A–C:

- 380 • Experiment 1A: Landslide 1 is released and interacts with the reservoir. The dam is as-
381 sumed stable and may therefore not be entrained.
- 382 • Experiment 1B: Again, Landslide 1 is released and interacts with the reservoir. However,
383 dam material is allowed to be entrained in this experiment.
- 384 • Experiment 1C: Landslide 2 is released and interacts with the dam and the reservoir. The
385 release from the input hydrograph I1 starts after 10 s and continues for a period of 130
386 seconds (see Fig. 5). Dam material is allowed to be entrained at all stages of the computa-
387 tional experiment.

388 All experiments are performed at a pixel size of 10 m and for a duration of $t_{\text{term}} = 300$ s; $\Delta t_{\text{out}} = 5$ s.
389 The solid and fluid discharges are continuously recorded at the output hydrograph profile O1
390 downstream. The stopping function is deactivated (see Table 3).

391 3.1.3 Results

392 Animations illustrating the time evolution of the flow heights in all three experiments are en-
393 closed in Supp. 1A, 1B, and 1C. Note that the description and analysis of the results is based on
394 output time steps with lengths of $\Delta t_{\text{out}} = 5$ s.

395 Fig. 6a–f illustrates the flow heights at selected points of time during Experiment 1A. The Land-
396 slide 1 (see Fig. 5a) impacts the backward portion of the reservoir after few seconds and generates
397 a water wave – oblique and perpendicular to the impact – that overtops the dam from $t = 50$ –55 s
398 onwards. The output hydrograph O1 starts recording discharge at $t = 65$ s, with the peak of the
399 first, major flood wave passing at $t = 75$ s ($Q_t = 8 \cdot 10^4 \text{ m}^3 \text{ s}^{-1}$; Fig. 6g). We note that the discharge and
400 the flow height recorded by the hydrograph do not strictly follow the same pattern, as the dis-
401 charge relates to a profile and the flow height relates to a point (see Fig. 2). Meanwhile the impact
402 wave is deflected at the dam and alleviates slowly. Further overtopping events caused by multiple
403 deflections of the alleviating wave occur mainly at the marginal parts of the dam at $t = 110, 150,$
404 $160, 200$ and 270 s, leading to smaller peaks in the output hydrograph ($Q_t = 1.5 \cdot 10^4 \text{ m}^3 \text{ s}^{-1}$ at
405 $t = 175$ s; $Q_t = 2.2 \cdot 10^3 \text{ m}^3 \text{ s}^{-1}$ at $t = 285$ s). The solid content passing the hydrograph profile is almost
406 negligible as all solid landslide material remains in the reservoir basin. At $t = 300$ s, the impact
407 wave in the lake has almost alleviated (see Supp. 1A).



408 Experiment 1B (Fig. 7) is identical to the Experiment 1A until the point when the impact wave
409 reaches the dam at $t = 50$ s. Entrainment of the dam starts with overtopping which sets on at the
410 lateral portions. Part of the dam is entrained during overtopping by the initial impact wave.
411 Whilst massive outflow from the reservoir occurs due to the decreased level of the dam crest, part
412 of the wave is deflected at the dam and pushed back towards the backward part of the reservoir,
413 inducing a system of secondary waves. The remaining dam material is entrained when hit by those
414 secondary waves. At $t = 200$ s the entire dam has disappeared and the reservoir starts emptying
415 completely. In contrast to Experiment 1A, due to the emptying process the system does not ap-
416 proach a static equilibrium after $t = 300$ s (see Supp. 1B).

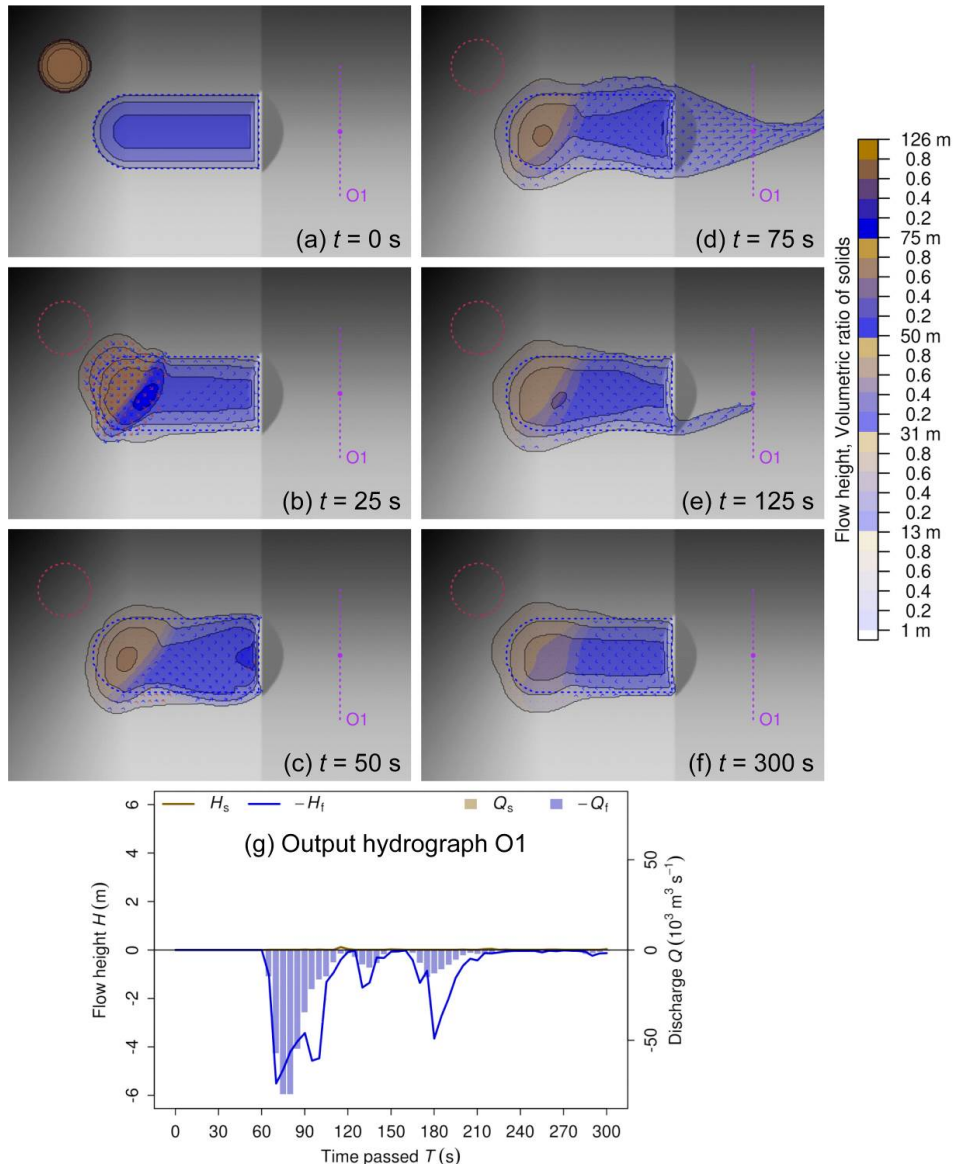
417 The temporal patterns of the simulated entrainment and wave propagation are clearly reflected in
418 the discharge recorded at the output hydrograph O1 (see Fig. 7g). As a consequence of dam over-
419 topping, fluid discharge at O1 starts increasing at $t = 65$ s and reaches a first peak at $t = 80$ s
420 ($Q_f = 5.1 \cdot 10^4 \text{ m}^3$). Solid discharge – a consequence of entrainment of the dam – starts slightly de-
421 layed, reaching a first peak roughly ten seconds later ($Q_s = 2.1 \cdot 10^4 \text{ m}^3 \text{ s}^{-1}$). A depression in both of
422 the discharge curves at $t = 155$ – 160 s indicates that the initial impact wave has passed through. A
423 second, larger peak of fluid discharge is simulated at $t = 195$ s ($Q_f = 1.0 \cdot 10^5 \text{ m}^3 \text{ s}^{-1}$). It occurs syn-
424 chronously with a second, smaller peak of solid discharge ($Q_s = 2.1 \cdot 10^4 \text{ m}^3 \text{ s}^{-1}$), indicating a high
425 degree of mixing of the solid and fluid components of the flow. The pronounced second peak of Q_f
426 is a consequence of the secondary waves in combination with the lowered level of the dam. After
427 the peak, Q_s slowly and unsteadily decreases (the entire dam has been entrained and the material
428 has passed through) whilst Q_f remains high. Due to the entrainment of the dam, the simulated dis-
429 charges are much higher than those computed in the Experiment 1A (see Fig. 6g).

430 In Experiment 1C (Fig. 8) Landslide 2 impacts the dam and the frontal part of the reservoir less
431 than 10 s after release. The proximal portion of the dam is entrained rapidly. The right part of the
432 landslide moves outside of the reservoir in downstream direction. Consequently, the solid dis-
433 charge at the output hydrograph O1 starts at $t = 30$ s, reaching a peak of $Q_s = 2.9 \cdot 10^4 \text{ m}^3 \text{ s}^{-1}$ ten sec-
434 onds later (see Fig. 8g). Due to the high (75%) solid fraction of the landslide, the fluid discharge is
435 lower at that time ($Q_f = 1.0 \cdot 10^4 \text{ m}^3 \text{ s}^{-1}$). The left part of the landslide interacts with the reservoir,
436 causing overtopping at the distal portion of the dam. This results in the increase of fluid discharge
437 recorded at O1, culminating at $t = 60$ s when the solid discharge is already decreasing
438 ($Q_s = 2.9 \cdot 10^4 \text{ m}^3 \text{ s}^{-1}$). The immediate impact of the initial landslide and the resulting impact wave
439 on O1 has largely alleviated after $t = 100$ s in terms of discharge, even though the total flow height
440 remains at $H > 2$ m. This means that the flow material largely remains in place at O1.

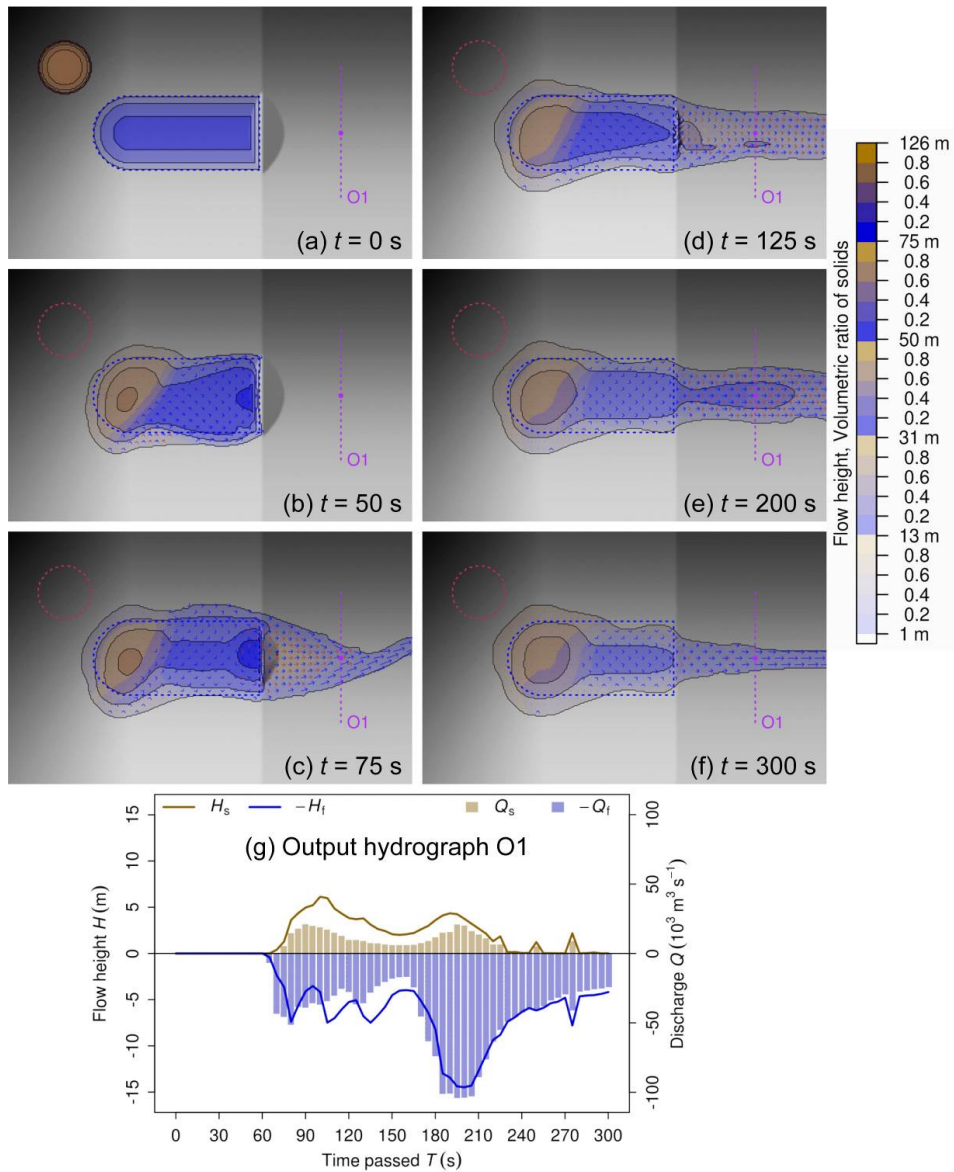
441 From $t = 30$ s onwards the flow released through the input hydrograph I1 (see Fig. 5b) pushes the
442 reservoir water towards NE. The remnants of the dam are overtopped by the resulting inhomoge-
443 neous solid-fluid mixture (including material originating from Landslide 2), leading to substantial
444 further entrainment. In contrast to Experiment 1B, however, the dam is not completely entrained.
445 The wave starts influencing the discharge recorded at O1 at $t = 135$ s. A subsequent steady increase
446 of solid and fluid discharge leads to a broad peak recorded at $t = 230$ – 250 s ($Q_s = 1.3 \cdot 10^4 \text{ m}^3 \text{ s}^{-1}$;
447 $Q_f = 3.7 \cdot 10^4 \text{ m}^3 \text{ s}^{-1}$). At that time the hydrograph indicates a well-mixed flow with $\alpha_s \approx 0.25$, com-



448 posed of fluid from the reservoir, solid-fluid mixtures from the landslide and the hydrograph re-
 449 lease, and solid material from the dam (see Fig. 5a). The solid and fluid discharge steadily decrease
 450 after $t = 250$ s, reflecting the termination of the hydrograph release and the emptying of the reser-
 451 voir. However, emptying of the reservoir operates much more slowly than in Experiment 1B due to
 452 the comparatively high solid content of the system which is still far away from a static equilib-
 453 rium after $t = 300$ s (see Supp. 1C).

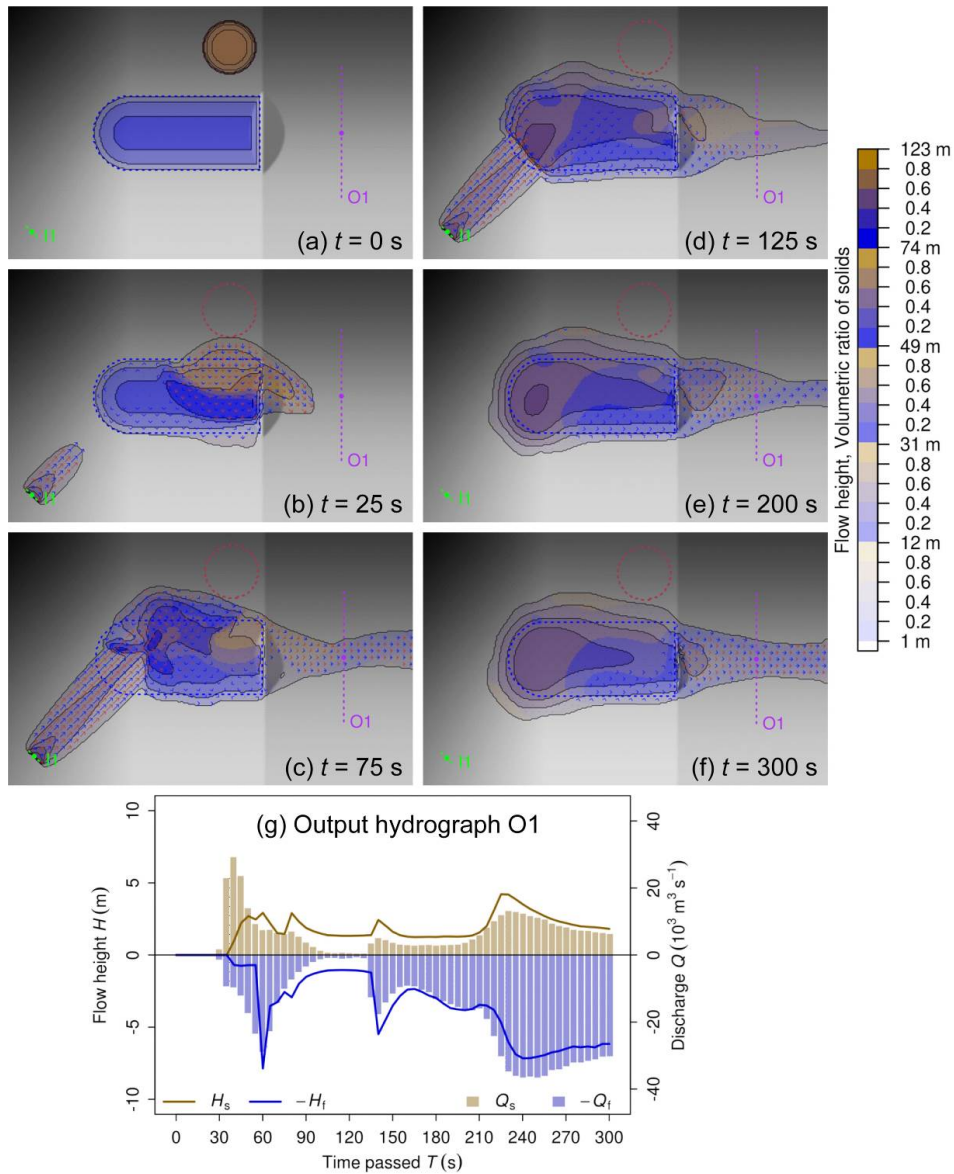


454
 455 Figure 6 Key results of Experiment 1A. (a)–(f) Sequence of simulated flow heights and solid ratios
 456 at selected points of time; see Supp. 1A for animations of flow height and kinetic energy sequenc-
 457 es; (g) output hydrograph O1 (see Fig. 5a).



458
 459
 460
 461

Figure 7 Key results of Experiment 1B. (a)–(f) Sequence of simulated flow heights and solid ratios at selected points of time; see Supp. 1B for animations of flow height and kinetic energy sequences; (g) output hydrograph O1 (see Fig. 5a).



462
 463 Figure 8 Key results of Experiment 1C. (a)–(f) Sequence of simulated flow heights and solid ratios
 464 at selected points of time; see Supp. 1C for animations of flow height and kinetic energy sequenc-
 465 es; (g) output hydrograph O1 (see Fig. 5a).
 466

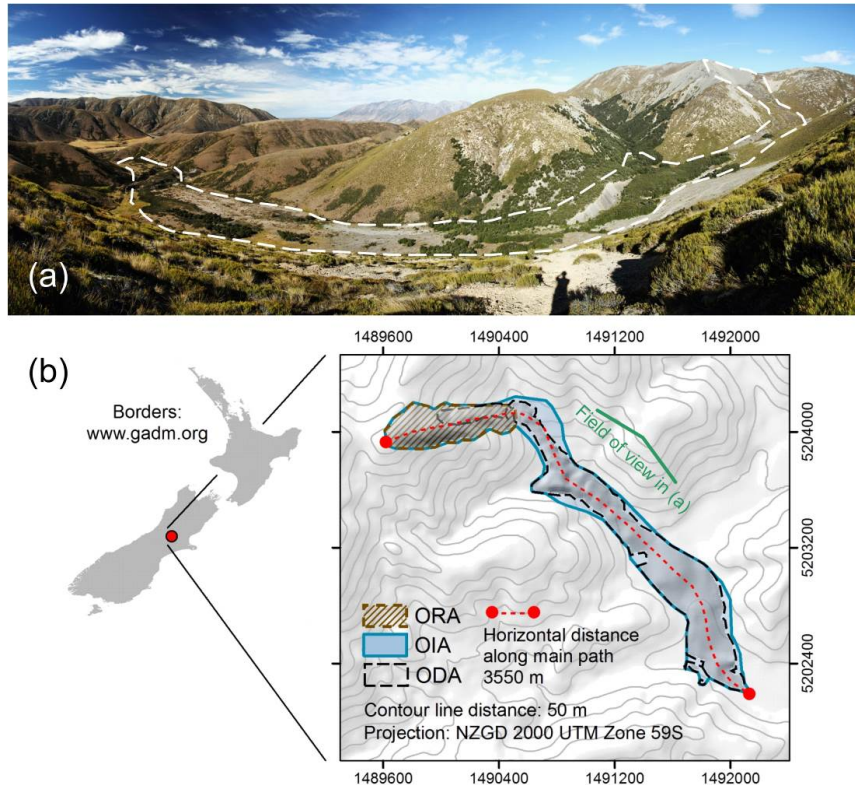


467 3.2 Experiment 2: Acheron rock avalanche, New Zealand

468 3.2.1 Event description

469 The Acheron rock avalanche in Canterbury, New Zealand (Fig. 9), occurred approx. 1,100 years
470 BP (Smith et al., 2006). It is characterized by sharp bending of the flow path, a limited degree of
471 spreading into the lateral valleys and a high mobility (travel distance: 3,550 m; measured angle of
472 reach: 11.62°). It was used as a test event for the computational tool *r.randomwalk* (Mergili et al.,
473 2015).

474 We use a 10 m resolution DEM derived by stereo-matching of aerial photographs. ODA and OIA
475 are derived from field and imagery interpretation as well as from data published by Smith et al.
476 (2006). The OIA possibly underrepresents the real impact area as it might exclude some lateral and
477 run-up areas of the rock avalanche not any more recognizable as such in the field. The distribu-
478 tion of release and deposition heights and an estimated release volume of 6.4 million m³ are de-
479 duced from the reconstruction of the pre-event topography. According to this reconstruction, the
480 maximum release height is 78.7 m whilst the maximum deposition height is 25.9 m.



481
482
483

Figure 9 The Acheron rock avalanche. (a) Oblique view; the view point is indicated in (b) illustrating the location and the main elements of the rock avalanche; ORA = Observed release area.



484 3.2.2 Modelling strategy and parameterization

485 Preliminary tests have shown that the simulation results of r.avaflow are potentially sensitive to
486 variations in the initial solid fraction α_{s0} and the basal friction angle δ , parameters which are un-
487 certain in many real-world applications. We perform two computational experiments for the Ach-
488 eron rock avalanche:

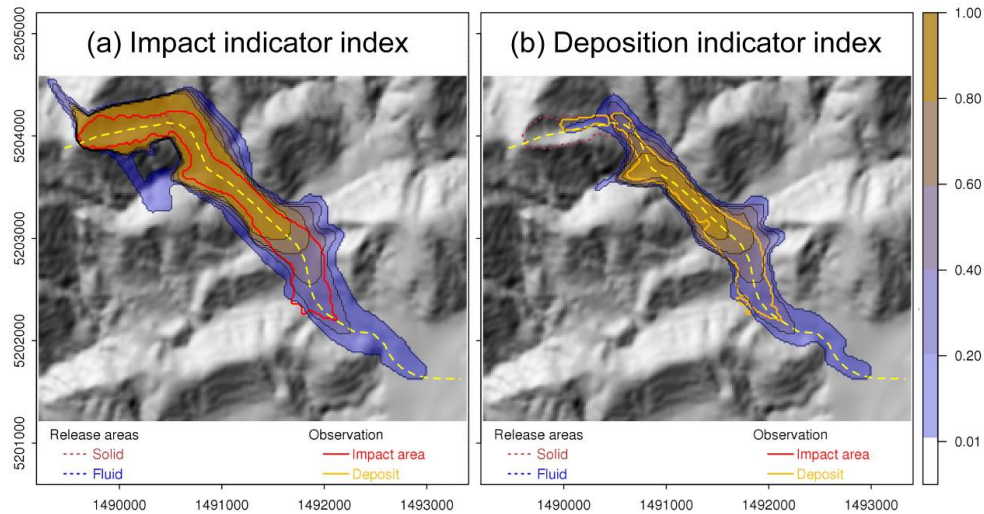
- 489 1. Experiment 2A: *III* and *DII* are computed from a set of 121 model runs. Thereby, α_{s0} is
490 varied from 0.5–0.9, and δ is varied from 15–25° (see Table 2). The variation is done in a
491 controlled way assuming a uniform probability density function i.e. a regular grid with 11
492 grid points in each dimension is laid over the two-dimensional parameter space. *III* is then
493 evaluated against the OIA, and *DII* is evaluated against the ODA. α_{s0} and δ are optimized
494 in terms of ΔL , *FoC*, *CSI*, and *D2PC* derived from H_D and the ODA.
- 495 2. Experiment 2B: r.avaflow simulation with the optimized values of α_{s0} and δ .

496 Both experiments are conducted at a pixel size of 20 m. Entrainment is not considered whilst stop-
497 ping is included (see Table 3). All flow parameters except for δ are kept constant (see Table 2).

498 3.2.3 Results

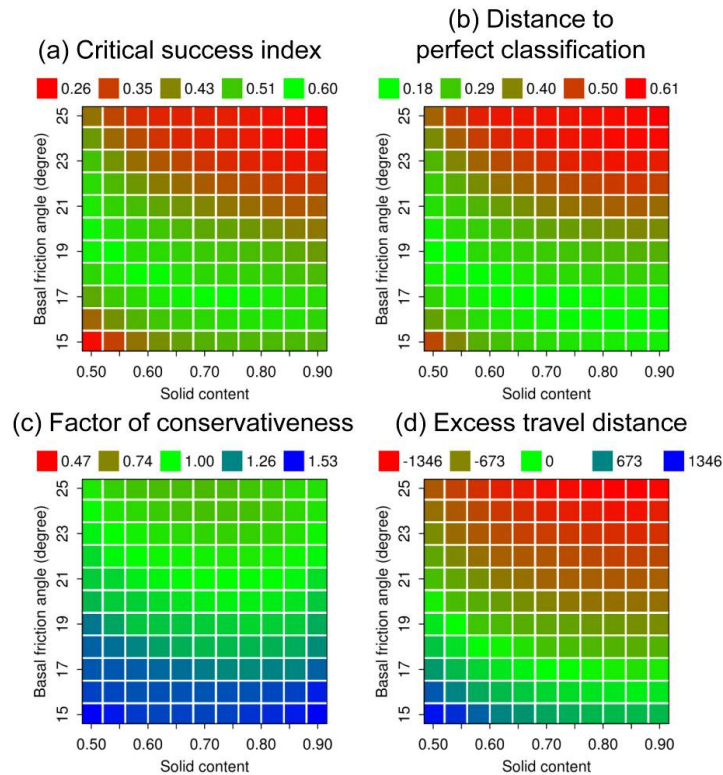
499 Fig. 10 illustrates *III* and *DII* derived with the parameter settings shown in the Tables 2 and 3 (Ex-
500 periment 2A). AUC_{ROC} is 0.830 with regard to *III* and 0.838 with regard to *DII*. In general, those
501 areas with high values of *III* coincide with the OIA, whilst those areas with lower values of *III* lie
502 close to the margins or outside of the OIA. The performance of *III* suffers from the motion of
503 small portions of the simulated avalanche in the wrong (N) direction and from excessive lateral
504 spreading and run-up in the upper part, observed for all tested combinations of α_{s0} and δ (high
505 values of *III*; see Fig. 10a). However, one has to consider that the event occurred hundreds of years
506 ago and run-up may have occurred even though it is not any more recognizable in the field and
507 therefore excluded from the OIA. High values of *DII* are fairly constrained to those pixels within
508 the ODA (see Fig. 10b) which is most probably better defined than the OIA. Those areas with
509 lower, but non-zero values of *III* or *DII* both reach well beyond the reference areas. Particularly
510 the travel distance appears highly sensitive to the choice of α_{s0} and δ .

511 We now focus on the components of the *DII* map and evaluate the performance of the deposition
512 maps simulated with the various combinations of α_{s0} and δ against the ODA. Fig. 11 illustrates the
513 dependency of the model performance (defined by the parameters summarized in Table 4) on the
514 combination of α_{s0} and δ employed for a given model run. All four parameters clearly indicate
515 that, within the ranges tested, the model results are sensitive to both δ and α_{s0} . ΔL , *CSI*, and *D2PC*
516 display their optima near to $\delta = 17^\circ$ as long as $\alpha_s \geq 0.7$. With higher fluid content, the optimum
517 value of δ increases, arriving at 20° with $\alpha_{s0} = 0.5$ (see Fig. 11a, b and d). This pattern appears plau-
518 sible as far as a higher fluid content is supposed to increase the mobility of the flow, compensating
519 for higher values of δ . However, values of $\alpha_{s0} < 0.7$ are not plausible for a rock avalanche of this
520 type. For $\alpha_s \geq 0.7$ *FoC* displays its optimum of 1.0 at $\delta \geq 21^\circ$, depending on α_{s0} . $C \approx 1.25$ for the val-
521 ue of δ where the other parameters reach their optimum (see Fig. 11c). This would be fine for
522 many applications in practice where slightly conservative results are desirable.



523
 524
 525

Figure 10 Results of Experiment 2A: (a) Impact indicator index III and (b) deposition indicator index DII derived for the Acheron rock avalanche.

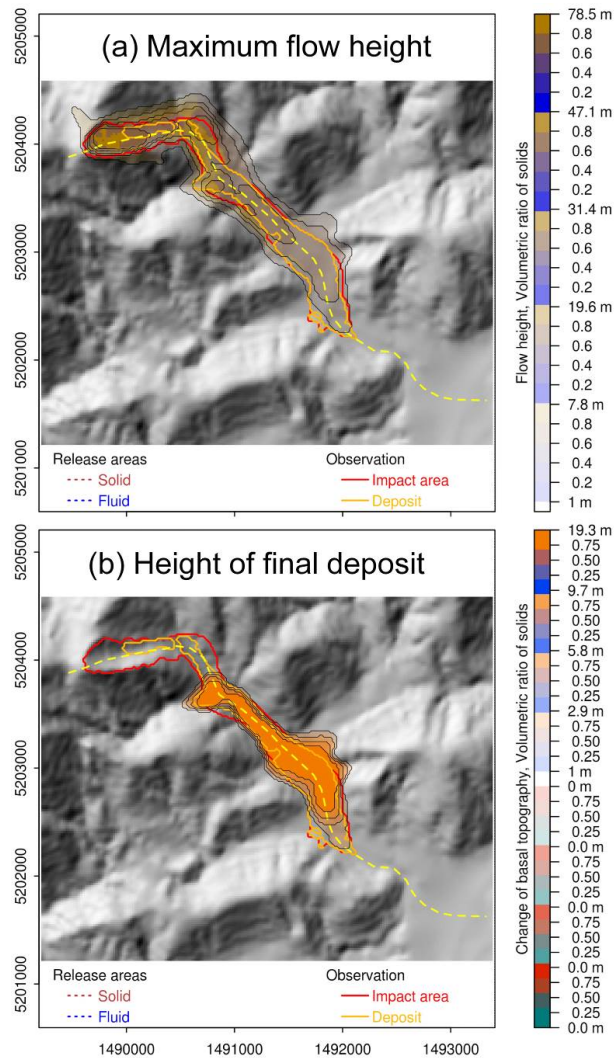


526
 527
 528
 529

Figure 11 Validation and optimization of DII for the Acheron rock avalanche: (a) Critical success index CS_i ; (b) Distance to perfect classification D_2PC ; (c) Factor of conservativeness FoC ; (d) Excess travel distance ΔL .



530 Consequently, we consider $\delta = 17^\circ$ and $\alpha_{s0} = 0.8$ – in addition to the parameter values given in Ta-
 531 ble 2 – useful for back-calculating the Acheron rock avalanche. The simulation is repeated with
 532 exactly this combination (Experiment 2B). Fig. 12 shows the maps of H_{Max} and H_b , both corre-
 533 sponding reasonably well to the OIA and the ODA, respectively. The slightly larger simulated
 534 than observed deposit (see Fig. 12b) corresponds to $FoC \approx 1.25$, the almost perfect correspondence
 535 of the observed and simulated termini corresponds to $\Delta L \approx 0$. This means that the fact that the re-
 536 sult is rather conservative than non-conservative ($FoC > 1$) relates to lateral spreading rather than
 537 to the travel distance of the rock avalanche. Supp. 2 illustrates the time evolution of the flow
 538 height in Experiment 2B.



539
 540 Figure 12 Results of Experiment 2B. (a) Maximum flow height H_{Max} ; (b) Height of final deposit H_b .



541 **4 Discussion**

542 The key purpose of the present article is to provide a general introduction to the key functional-
543 ities of the computational tool *r.avaflow*. Thereby, the simulated patterns of flow height in Exper-
544 iment 1 (see Sect. 3.1) appear plausible, and the correspondence of the observed and simulated
545 deposition areas in Experiment 2B (see Sect. 3.2) appears reasonable. Yet, these experiments can
546 neither replace model validation efforts with observed process chains or interactions, nor thor-
547 ough multi-parameter sensitivity analysis and optimization efforts, which will both be the subjects
548 of future research. Fully documented two-phase process chains with readily available pre- and
549 post-event DTMs are scarce. Preliminary *r.avaflow* results for the 2012 Santa Cruz multi-lake out-
550 burst flood in the Cordillera Blanca, Peru (Emmer et al., 2016) are, however, promising.

551 Experiment 2 serves for the demonstration of the parameter sensitivity analysis and optimization
552 functions of *r.avaflow*. The outcomes may be different when changing the pixel size or any of the
553 flow parameter values (see Table 2). Making *r.avaflow* fit for forward predictions will require a
554 thorough multi-parameter sensitivity analysis and optimization campaign involving a large num-
555 ber and variety of well-documented events. Thereby we aim at obtaining guiding parameter val-
556 ues – or, more appropriately, guiding parameter ranges – for mass flow processes of different types
557 and magnitudes. Approaches to perform such analyses are readily available, and some of them can
558 be directly coupled to *r.avaflow* (Fischer, 2013; Fischer et al., 2015; Aaron et al., 2016; Krenn et al.,
559 2016). However, due to the complex nature of two-phase mixture flows, *r.avaflow* depends on a
560 relatively large number of flow parameters, a fact that represents a particular challenge in terms of
561 the computational resources as well as in terms of visualization and interpretation of the results of
562 multi-parameter studies.

563 *r.avaflow* represents a modular framework, allowing for the future enhancement of its particular
564 components. One issue concerns the numerical implementation of the two-phase model equa-
565 tions, combining topography-following coordinates with the quadratic grid of the GIS raster data
566 (see Sect. 2.3). As in comparable simulation tools (e.g. Christen et al., 2010a, b; Hergarten and
567 Robl, 2015), approximations are currently used for coordinate transformation in *r.avaflow*. In ad-
568 dition the numerical scheme employed could further be enhanced to effectively incorporate the
569 complementary functions outlined in Table 3 in a fully consistent way. Extensions of similar
570 schemes have been tested for generic examples (e.g., Zhai et al., 2015) and could serve as a valua-
571 ble basis also to implement a mechanical model for entrainment and deposition (Pudasaini and
572 Fischer, 2016). On the one hand such a model may build on existing concepts (e.g. Fraccarollo and
573 Capart, 2002; Sovilla et al., 2006; Medina et al., 2008; Armanini et al., 2009; Crosta et al., 2009;
574 Hungr and McDougall, 2009; Le and Pitman, 2009; Iverson, 2012; Pirulli and Pastor, 2012). On the
575 other hand, it requires some fundamentally new ideas with regard to deposition.

576 **5 Conclusions and outlook**

577 We have introduced *r.avaflow*, a multi-functional open source GIS application for simulating two-
578 phase mass flows, process chains and interactions. The outcomes of two computational experi-



579 ments have revealed that `r.avaflow` (i) has the capacity to simulate complex solid-fluid process in-
580 teractions in a plausible way; and (ii) after the optimization of the basal friction angle and the solid
581 content of the release mass, reasonably reproduces the observed deposition area of a documented
582 rock avalanche. However, it was out of scope of the present work to validate the results obtained
583 for complex process interactions against observed real-world data, or even to conduct a compre-
584 hensive multi-parameter optimization campaign. Such efforts will be the next step towards mak-
585 ing `r.avaflow` ready for the forward prediction of possible future mass flow events. Thereby we
586 will attempt to establish guiding parameter values for different types of processes and process
587 magnitudes.

588 At the same time we have identified a certain potential for the future enhancement of some the
589 components of `r.avaflow`. The key challenges will consist in (i) integrating the model equations in
590 an up-to-date numerical scheme, allowing to directly include the complementary functions; and
591 (ii) replacing or complementing the empirical entrainment model with a mechanical model for
592 entrainment and deposition.

593 **Code availability**

594 The model codes, a user manual, the scripts used for starting the computational experiments pre-
595 sented in Sect. 3, and the GRASS locations with the spatial data necessary for reproducing the ex-
596 periments are available at <http://www.avaflow.org>.

597 **Acknowledgements**

598 The work was conducted as part of the international cooperation project “A GIS simulation model
599 for avalanche and debris flows (`avaflow`)” supported by the German Research Foundation (DFG,
600 project number PU 386/3-1) and the Austrian Science Fund (FWF, project number I 1600-N30).
601 We are grateful to Matthias Benedikt and Matthias Rauter for comprehensive technical support.

602 **References**

- 603 Aaron, J., Hungr, O., and McDougall, S.: Development of a systematic approach to calibrate equiv-
604 alent fluid runout models. In: Aversa, S., Cascini, L., Picarelli, L., and Scavia, C. (eds): *Landslides
605 and Engineered Slopes. Experience, Theory and Practice. Proc. 12th International Symposium of
606 Landslides, Napoli, Italy, 285–293*, CRC Press, Boca Raton, London, New York, Leiden, 2016.
- 607 Armanini, A., Fraccarollo, L., and Rosatti, G.: Two-dimensional simulation of debris flows in erod-
608 ible channels. *Comput. Geosci.*, 35, 993–1006, 2009.
- 609 Berger, C., McArdell, B. W., and Schlunegger, F.: Sediment transfer patterns at the Illgraben
610 catchment, Switzerland: Implications for the time scales of debris flow activities. *Geomorphology*,
611 125(3), 421–432, 2011.
- 612 Chen, H., Crosta, G. B., and Lee, C. F.: Erosional effects on runout of fast landslides, debris flows
613 and avalanches: A numerical investigation. *Geotechnique*, 56, 305–322, 2006.



- 614 Christen, C., Bartelt, P., and Kowalski, J.: Back calculation of the In den Arelen avalanche with
615 RAMMS: interpretation of model results. *Ann. Glaciol.*, 51(54), 161–168, 2010a.
- 616 Christen, M., Kowalski, J., and Bartelt, B.: RAMMS: Numerical simulation of dense snow ava-
617 lanches in three-dimensional terrain. *Cold Reg. Sci. Technol.*, 63, 1–14, 2010b.
- 618 Courant, R., Friedrichs, K., and Lewy, H.: On the partial difference equations of mathematical
619 physics. *IBM J.*, 11(2), 215–234, 1967.
- 620 Crosta, G. B., Imposimato, S., and Roddeman, D.: Numerical modelling of entrainment/deposition
621 in rock and debris-avalanches. *Eng. Geol.*, 109, 135–145, 2009.
- 622 Davis, S. F.: Simplified second-order Godunov-type methods. *SIAM J. Sci. Stat. Comput.*, 9(3),
623 445–473, 1988.
- 624 Denlinger, R. P., and Iverson, R. M.: Granular avalanches across irregular three-dimensional ter-
625 rain: 1. Theory and computation. *J. Geophys. Res.*, 109, F01014, 2004.
- 626 Emmer, A., Mergili, M., Juricová, A., Cochachin, A., and Huggel, C.: Insights from analyzing and
627 modelling cascading multi-lake outburst flood events in the Santa Cruz Valley (Cordillera Blanca,
628 Perú). *Geophys. Res. Abstr.*, 18, 2181, 2016.
- 629 Evans, S. G., Bishop, N. F., Fidel Smoll, L., Valderrama Murillo, P., Delaney, K. B., and Oliver-
630 Smith, A.: A re-examination of the mechanism and human impact of catastrophic mass flows origi-
631 nating on Nevado Huascarán, Cordillera Blanca, Peru in 1962 and 1970. *Engin. Geol.*, 108, 96–118,
632 2009.
- 633 Fischer, J.-T.: A novel approach to evaluate and compare computational snow avalanche simula-
634 tion. *Nat. Haz. Earth Syst. Sci.*, 13, 1655–1667, 2013.
- 635 Fischer, J.-T., Kofler, A., Fellin, W., Granig, M., and Kleemayr, K.: Multivariate parameter optimi-
636 zation for computational snow avalanche simulation in 3d terrain. *J. Glaciol.*, 61(229), 875–888,
637 2015.
- 638 Formetta, G., Capparelli, G., and Versace, P.: Evaluating performances of simplified physically
639 based models for landslide susceptibility. *Hydrol. Earth Syst. Sci. Discuss.*, 12, 13217–13256, 2015.
- 640 Fraccarollo, L., and Capart, H.: Riemann wave description of erosional dam-break flows. *J. Fluid
641 Mech.*, 461, 183–228, 2002.
- 642 Gamma, P.: Dfwalk – Murgang-Simulationsmodell zur Gefahrenzonierung. *Geographica Bernen-
643 sia*, G66, 2000.
- 644 GRASS Development Team: Geographic Resources Analysis Support System (GRASS) Software,
645 Version 7.0. Open Source Geospatial Foundation, 2015. <http://grass.osgeo.org>, last access: 25 July
646 2016.
- 647 Grigoriyan, S. S., Eglit, M. E., and Yakimov, Y. L.: A new formulation and solution of the problem
648 of the motion of a snow avalanche. *Trudy Vycokogornogo Geofiziceskogo Instituta*, 12, 104–113,
649 1967.



- 650 Guzzetti, F.: Landslide hazard and risk assessment. PhD Dissertation, Bonn, 2006.
- 651 Hergarten, S., and Robl, J.: Modelling rapid mass movements using the shallow water equations in
652 Cartesian coordinates. *Nat. Hazards Earth Syst. Sci.*, 15(3), 671–685, 2015.
- 653 Horton, P., Jaboyedoff, M., Rudaz, B., and Zimmermann, M.: Flow-R, a model for susceptibility
654 mapping of debris flows and other gravitational hazards at a regional scale. *Nat. Haz. Earth Syst.
655 Sci.*, 13, 869–885, 2013.
- 656 Huggel, C., Zraggen-Oswald, S., Haeberli, W., Kääh, A., Polkvoj, A., Galushkin, I., and Evans,
657 S.G.: The 2002 rock/ice avalanche at Kolka/Karmadon, Russian Caucasus: assessment of extraordi-
658 nary avalanche formation and mobility, and application of QuickBird satellite imagery. *Nat. Haz.
659 Earth Syst. Sci.*, 5, 173–187, 2005.
- 660 Hungr, O., and McDougall, S.: Two numerical models for landslide dynamic analysis. *Comput.
661 Geosci.*, 35(5), 978–992, 2009.
- 662 Hungr, O.: A model for the runout analysis of rapid flow slides, debris flows, and avalanches. *Can.
663 Geotech. J.*, 32, 610–623, 1995.
- 664 Hungr, O., McDougall, S., and Bovis, M.: Entrainment of material by debris flows. In: Jakob, M.,
665 and Hungr, O. (eds.): *Debris-flow hazards and related phenomena*, 135–158, Springer, Berlin, Hei-
666 delberg, 2005b.
- 667 Hungr, O., and Evans, S. G.: Entrainment of debris in rock avalanches: an analysis of a long run-
668 out mechanism. *Geol. Soc. Am. Bull.*, 116(9–10), 1240–1252, 2004.
- 669 Hungr, O., Corominas, J., and Eberhardt, E.: State of the Art paper: Estimating landslide motion
670 mechanism, travel distance and velocity. In: Hungr, O., Fell, R., Couture, R., Eberhardt, E. (eds.):
671 *Landslide Risk Management. Proceedings of the International Conference on Landslide Risk Man-
672 agement*, Vancouver, Canada, 31 May – 3 June 2005, 129–158, 2005a.
- 673 Hutter, K., and Schneider L.: Important Aspects in the Formulation of Solid-Fluid Debris-Flow
674 models. Part I: Thermodynamic Implications. *Continuum Mech. Thermodyn.*, 22(5), 363–390,
675 2010a.
- 676 Hutter, K., and Schneider L.: Important Aspects in the Formulation of Solid-Fluid Debris-Flow
677 models. Part II: Constitutive Modelling. *Continuum Mech. Thermodyn.*, 22(5), 391–411, 2010b.
- 678 Iverson, R. M.: The physics of debris flows. *Rev. Geophys.*, 35, 245–296, 1997.
- 679 Iverson, R. M.: Elementary theory of bed-sediment entrainment by debris flows and avalanches, J.
680 *Geophys. Res.*, 117, F03006, 2012.
- 681 Iverson, R. M., and Denlinger, R. P.: Flow of variably fluidised granular masses across three-
682 dimensional terrain. I: Coulomb mixture theory. *J. Geophys. Res.*, 106, 537–552, 2001.
- 683 Kafle, J., Pokhrel, P. R., Khattri, K. B., Kattel, P., Tuladhar, B. M., and Pudasaini, S. P.: Landslide-
684 generated tsunami and particle transport in mountain lakes and reservoirs. *Ann. Glaciol.*, 57(71),
685 232–244, 2016.



- 686 Kattel, P., Khattri, K. B., Pokhrel, P. R., Kafle, J., Tuladhar, B. M., and Pudasaini, S. P.: Simulating
687 glacial lake outburst floods with a two-phase mass flow model. *Ann. Glaciol.*, 57(71), 349–358,
688 2016.
- 689 Kowalski, J., and McElwaine, J. N.: Shallow two-component gravity-driven flows with vertical
690 variation. *J. Fluid Mech.*, 714, 434–462, 2013.
- 691 Krenn, J., Mergili, M., Fischer, J.-T., Frattini, P., and Pudasaini, S. P.: Optimizing the parameteri-
692 zation of mass flow models. In: Aversa, S., Cascini, L., Picarelli, L., and Scavia, C. (eds): *Landslides
693 and Engineered Slopes. Experience, Theory and Practice. Proc. 12th International Symposium of
694 Landslides, Napoli, Italy, 1195–1203*, CRC Press, Boca Raton, London, New York, Leiden, 2016.
- 695 Le, L., and Pitman, E. B.: A model for granular flows over an erodible surface. *SIAM J. Appl.
696 Math.*, 70, 1407–1427, 2009.
- 697 Lied, K., and Bakkehøi, S.: Empirical calculations of snow-avalanche run-out distance based on
698 topographic parameters. *J. Glaciol.*, 26, 165–177, 1980.
- 699 Mangeney, A., Bouchut, F., Lajeunesse, E., Aubertin, A., Vilotte, J. P., and Pirulli, M.: On the use
700 of Saint Venant equations to simulate the spreading of a granular mass. *J. Geophys. Res.*, 110,
701 B09103, 2005.
- 702 Mangeney, A., Vilotte, J. P., Bristeau, M. O., Perthame, B., Bouchut, F., Simeoni, C., and Yerneni,
703 S.: Numerical modelling of avalanches based on Saint Venant equations using a kinetic scheme. *J.
704 Geophys. Res., Solid Earth*, 108, (B11)2527, 2003.
- 705 McDougall, S., and Hungr, O.: A Model for the Analysis of Rapid Landslide Motion across Three-
706 Dimensional Terrain. *Canadian Geotech. J.*, 41, 1084–1097, 2004.
- 707 McDougall, S., and Hungr, O.: Dynamic modeling of entrainment in rapid landslides. *Canadian
708 Geotech. J.*, 42, 1437–1448, 2005.
- 709 Medina, V., Hürlimann, M., and Bateman, A.: Application of FLATModel, a 2D finite volume
710 code, to debris flows in the northeastern part of the Iberian Peninsula. *Landslides*, 5, 127–142,
711 2008.
- 712 Mergili, M., Schratz, K., Ostermann, A., and Fellin, W.: Physically-based modelling of granular
713 flows with Open Source GIS. *Nat. Haz. Earth Syst. Sci.*, 12, 187–200, 2012.
- 714 Mergili, M., Marchesini, I., Alvioli, M., Metz, M., Schneider-Muntau, B., Rossi, M., and Guzzetti,
715 F.: A strategy for GIS-based 3D slope stability modelling over large areas. *Geosci. Model Dev.*, 7,
716 2969–2982, 2014.
- 717 Mergili, M., Krenn, J., and Chu, H.-J.: *r.randomwalk v1*, a multi-functional conceptual tool for
718 mass movement routing. *Geosci. Model Dev.* 8, 4027–4043, 2015.
- 719 Nessayahu, H., and Tadmor, E.: Non-oscillatory central differencing for hyperbolic conservation
720 laws. *J. Comput. Phys.*, 87, 408–463, 1990.



- 721 Neteler, M., and Mitasova, H.: Open source GIS: a GRASS GIS approach. Springer, New York,
722 2007.
- 723 Pastor, M., Haddard, B., Sorbino, G., Cuomo, S., and Drempetic, V.: A depth-integrated, coupled
724 SPH model for flow-like landslides and related phenomena. *Int. J. Num. Anal. Meth. Geomech.*,
725 33, 143–172, 2009.
- 726 Pirulli, M., and Pastor, M.: Numerical study on the entrainment of bed material into rapid land-
727 slides. *Geotechnique*, 62, 959–972, 2012.
- 728 Pitman, E. B., and Le, L.: A two-fluid model for avalanche and debris flows. *Phil. Trans. R. Soc.*
729 A363, 1573–1601, 2005.
- 730 Pitman, E. B., Nichita, C. C., Patra, A. K., Bauer, A. C., Bursik, M., and Weber, A.: A model of gran-
731 ular flows over an erodible surface. *Discrete Contin. Dynam. Syst. B.*, 3, 589–599, 2003a.
- 732 Pitman, E. B., Nichita, C. C., Patra, A. K., Bauer, A., Sheridan, M., and Bursik, M.: Computing
733 granular avalanches and landslides. *Phys. Fluids*, 15(12), 3638–3646, 2003b.
- 734 Popinet, S.: An accurate adaptive solver for surface-tension-driven interfacial flows, *J. Comput.*
735 *Phys.*, 228, 5838–5866, 2009.
- 736 Pudasaini, S. P.: A general two-phase debris flow model, *J. Geophys. Res.*, 117, F03010, 2012.
- 737 Pudasaini, S. P.: Dynamics of submarine debris flow and tsunami. *Acta Mech.*, 225, 2423,
738 doi:10.1007/s00707-014-1126-0, 2014.
- 739 Pudasaini, S. P., and Fischer, J.-T.: A new two-phase erosion-deposition model for mass flows. *Ge-*
740 *ophys. Res. Abstr.*, 18, 4424, 2016.
- 741 Pudasaini, S. P., and Hutter, K.: *Avalanche Dynamics: Dynamics of rapid flows of dense granular*
742 *avalanches*. Springer, Berlin, Heidelberg, 2007.
- 743 Pudasaini, S. P., and Krautblatter, M.: A two-phase mechanical model for rock-ice avalanches. *J.*
744 *Geophys. R.: Earth Surf.*, 119(10), 2272–2290, 2014.
- 745 Pudasaini, S. P., Wang, Y., and Hutter, K.: Modelling debris flows down general channels. *Nat.*
746 *Hazards Earth Syst. Sci.*, 5(6), 799–819, 2005.
- 747 Pudasaini, S. P., Wang, Y., Sheng, L.-T., Hsiau, S.-S., Hutter, K., and Katzenbach, R.: Avalanching
748 granular flows down curved and twisted channels: Theoretical and experimental results. *Phys.*
749 *Fluids*, 20, 073302, 2008.
- 750 R Core Team.: *R: A Language and Environment for Statistical Computing*. R Foundation for Statis-
751 *tistical Computing*, Vienna, Austria, <http://www.R-project.org>, last access: 25 July 2016.
- 752 Reid, M. E., Iverson, R. M., Logan, M., Lahusen, R.G., Godt, J.W., and Griswold, J.P.: Entrain-
753 ment of bed sediment by debris flows: results from large-scale experiments. In: Genevois, R.,
754 Hamilton, D. L., and Prestininzi, A. (eds.): *Proc. 5th International Conference on Debris-Flow*
755 *Hazards Mitigation: Mechanics, Prediction and Assessment*, Padua, Italy (Italian Journal of Engi-
756 *neering Geology and Environment – Book*), 367-374, La Sapienza, Rome, 2011.



- 757 Rickenmann, D., Weber, D., and Stepanov, B.: Erosion by debris flows in field and laboratory ex-
758 periments. In: Rickenmann, D., and Chen, C.-L. (eds.): Proc. 3rd International Conference on
759 Debris-Flow Hazards Mitigation: Mechanics, Prediction, and Assessment, Davos, Switzerland,
760 883–894. Millpress, Rotterdam, 2003.
- 761 Sampl, P., and Zwinger, T.: Avalanche Simulation with SAMOS. *Ann. Glaciol.*, 38, 393–398, 2004.
- 762 Savage, S. B., and Hutter, K.: The motion of a finite mass of granular material down a rough in-
763 cline. *J. Fluid Mech.*, 199, 177–215, 1989.
- 764 Savage, S. B., and Iverson, R. M.: Surge dynamics coupled to pore-pressure evolution in debris
765 flows. In: Rickenmann, D., and Chen, C.-L. (eds.): Proc. 3rd International Conference on Debris-
766 Flow Hazards Mitigation: Mechanics, Prediction and Assessment, Davos, Switzerland, 503–514.
767 Millpress, Rotterdam, 2003.
- 768 Smith, G. M., Davies, T. R., McSaveney, M. J., and Bell, D. H.: The Acheron rock avalanche, Can-
769 terbury, New Zealand – morphology and dynamics. *Landslides*, 3, 62–72, 2006.
- 770 Sovilla, B., Burlando, P., and Bartelt, P.: Field experiments and numerical modeling of mass en-
771 trainment in snow avalanches. *J. Geophys. Res.*, 111, F03007, 2006.
- 772 Tai, Y. C., Noelle, S., Gray, J. M. N. T., and Hutter, K.: Shock-capturing and front-tracking meth-
773 ods for granular avalanches. *J. Comput. Phys.*, 175, 269–301, 2002.
- 774 Takahashi, T.: *Debris Flow*. IAHR Monograph Series, Balkema, The Netherlands, 1991.
- 775 Toro, E. F.: Riemann problems and the waf method for solving the twodimensional shallow water
776 equations. *Philos. Trans. R. Soc. London A*, 338, 43–68, 1992.
- 777 Van Westen, C. J., van Asch, T. W. J., and Soeters, R.: Landslide hazard and risk zonation : why is
778 it still so difficult? *Bull. Eng. Geol. Environ.*, 65(2), 176–184, 2005.
- 779 Voellmy, A.: Über die Zerstörungskraft von Lawinen. *Schweizerische Bauzeitung* 73, 159–162,
780 212–217, 246–249, 280–285, 1955.
- 781 Wang, Y., Hutter, K., and Pudasaini, S. P.: The Savage-Hutter theory: A system of partial differen-
782 tial equations for avalanche flows of snow, debris, and mud. *J. Appl. Math. Mech.*, 84, 507–527,
783 2004.
- 784 Wichmann, V., and Becht, M.: Modelling of Geomorphic Processes in an Alpine Catchment. In:
785 Proceedings of the 7th International Conference on GeoComputation, Southampton. 14 pp., 2003.
- 786 Zhai, Q., Zhang, R., and Wang, X.: A hybridized weak Galerkin finite element scheme for the
787 Stokes equations. *Sci. China Math.*, 58(11), 2455–2472, 2015.